PHYSICS

Frequency-domain study of nonthermal gigahertz phonons reveals Fano coupling to charge carriers

Thomas Vasileiadis[1,2], Heng Zhang[1], Hai Wang[1], Mischa Bonn[1], George Fytas[1]*, Bartlomiej Graczykowski[1,2]*

Telecommunication devices exploit hypersonic gigahertz acoustic phonons to mediate signal processing with microwave radiation, and charge carriers to operate various microelectronic components. Potential interactions of hypersound with charge carriers can be revealed through frequency- and momentum-resolved studies of acoustic phonons in photoexcited semiconductors. Here, we present an all-optical method for excitation and frequency-, momentum-, and space-resolved detection of gigahertz acoustic waves in a spatially confined model semiconductor. Lamb waves are excited in a bare silicon membrane using femtosecond optical pulses and detected with frequency-domain micro-Brillouin light spectroscopy. The population of photoexcited gigahertz phonons displays a hundredfold enhancement as compared with thermal equilibrium. The phonon spectra reveal Stokes–anti-Stokes asymmetry due to propagation, and strongly asymmetric Fano resonances due to coupling between the electron-hole plasma and the photoexcited phonons. This work lays the foundation for studying hypersonic signals in nonequilibrium conditions and, more generally, phonon-dependent phenomena in photoexcited nanostructures.

INTRODUCTION

Gigahertz (hypersonic) acoustic waves/phonons play an indispensable role in signal processing in wireless communication devices, sub-kelvin thermal transport management, optomechanics, and elastic evaluation of bulk and confined materials (*1*–*3*). Contrary to charge carriers, which exhibit confinement on nanometer and subnanometer length scales, the dispersion relations and the lifetimes of gigahertz phonons are strongly affected by spatial confinement in the submicrometer scale (*4*, *5*). This offers large flexibility for the engineering of hypersound using standard nanofabrication (*1*, *2*, *6*). The lifetimes of gigahertz acoustic phonons can surpass the nanosecond time scale depending on the degree of spatial confinement (*5*). All these characteristics of acoustic phonons are often used for signal processing in miniaturized devices (*7*). Mobile electronic devices contain several components that convert microwave radiation into acoustic signals with the aid of piezoelectric materials. The acoustic signals can be filtered, guided, or delayed in a limited space more easily than the parent electromagnetic waves (*8*) because of the group velocities of acoustic phonons (~$5{\cdot}10^3$ m/s), which are five orders of magnitude slower than of the photons.

In thermodynamic equilibrium, acoustic phonons are incoherent vibrations with small amplitudes. Hence, the detection schemes of thermal acoustic phonons in semiconducting nanostructures are limited to frequency-domain methods with poor signal-to-noise ratio. For practical applications, gigahertz acoustic phonons need to be amplified and brought into nonthermal, coherent states. The latter can be generated optically by ultrashort laser pulses and detected by time-resolved pump-probe optical spectroscopies (*9*), such as picosecond ultrasonics (*10*), transient grating technique (*11*, *12*), and asynchronous optical sampling (ASOPS) (*5*). Despite their indisputable usefulness, these techniques are limited in probing bulk waves, specific phonon momentum (*10*), or nonpropagating modes (*5*). Most often, the excitation involves the use of metallic transducers (*13*) or heterostructures (*14*), which limit flexibility in the design of the phononic devices.

Previously, micro-Brillouin light spectroscopy (BLS) has been combined with laser pumping and metallic transducers to generate acoustic waves, but this method was limited to bulk waves in insulating materials (*15*, *16*). An alternative optical approach for the excitation of hypersonic phonons is through optomechanical coupling in low-dimensional structures (*17*) harnessing the interaction of standing, acoustic waves with electromagnetic cavity modes (*18*). In most studies, nonthermal excitation of acoustic signals refers to surface acoustic waves (SAWs) (*19*) or bulk waves (*20*). The one-dimensional (1D) confined analog of SAWs, the so-called Lamb waves, has great potential as building blocks of filters and delay lines for 5G technologies (*21*). Sources of acoustic waves typically use piezoelectric materials, but nonpiezoelectric semiconductors, such as Si, gain increasing attention for applications based on strong photon-phonon interactions (*22*).

An important aspect that needs to be addressed is the coupling of gigahertz acoustic waves to other microscopic excitations that can generate losses and interferences. In semiconducting devices, gigahertz acoustic waves can coexist with charge carriers that are strongly confined near the band gap extrema. The relaxation of electrons and holes in this narrow region of the phase space can involve emission of minute amounts of energy and momentum in the form of acoustic phonons. The excitation of electrons and holes in semiconductors is known to generate coherent acoustic waves through the deformation potential mechanism (*10*). Therefore, an in-depth understanding of the coupling between acoustic waves and charge carriers can be beneficial to many applications that emerge at the interface of gigahertz acoustics and optoelectronics (*23*, *24*).

In this work, we study a model system exemplified by a 260-nm-thick single-crystal silicon membrane that hosts gigahertz acoustic waves and electron-hole excitations (*4*). Nonequilibrium, dilatational

[1]Max Planck Institute for Polymer Research, Ackermannweg 10, 55128 Mainz, Germany. [2]Faculty of Physics, Adam Mickiewicz University, Uniwersytetu Poznanskiego 2, 61-614 Poznan, Poland.
*Corresponding author. Email: fytas@mpip-mainz.mpg.de (G.F.); bartlomiej.graczykowski@amu.edu.pl (B.G.)

Lamb waves are excited and observed with space and momentum resolution using a hybrid experimental method termed pumped BLS. This technique combines pulsed photoexcitation at high repetition rate with micro–Brillouin light spectroscopy (μ-BLS) detection. Our approach offers a flexible transducer-free source and a sensitive detector of spatially confined, standing, and propagating gigahertz acoustic waves. Compared with spontaneous BLS, the photoexcited BLS signal is strongly enhanced, and the Lorentzian peak profiles turn to highly asymmetric Fano resonances. The latter manifests the interaction between discrete photoexcited phonons and the continuum of electron-hole pairs. The reported method is readily applicable to other narrow-band-gap semiconductors, heterostructures that contain semiconducting nanomembranes, and various other acoustic metamaterials.

RESULTS

Photoexcitation of Lamb waves and frequency-domain detection

The pump-probe setup used for the photoinduced amplification of gigahertz acoustic waves under 1D spatial confinement is illustrated in Fig. 1A. Femtosecond laser pulses (780 nm) pump the silicon membrane exciting electron-hole pairs and coherent acoustic phonons. The acoustic phonons are probed by means of a continuous wave (CW) laser light at 532 nm. The CW light is inelastically scattered by the acoustic waves, and the Doppler frequency–shifted scattered photons are resolved by μ-BLS in backscattering geometry. The negative (positive) frequency shift corresponds to phonon creation and Stokes scattering (phonon annihilation and anti-Stokes scattering). In the case of membranes, the BLS signal results from the superposition of the moving boundary (surface-ripple) mechanism and the photoelastic effect (*4*, *25*, *26*).

The photoexcited Lamb waves have S1 dilatational character (Fig. 1B) (*4*). The wave vector of detected phonons is parallel to the membrane surface with magnitude $k_{\parallel} = 4\pi\sin\theta/\lambda$. Here, $\lambda = 532$ nm is the wavelength of the probe light, and θ is the angle between the CW beam and the vector normal to the membrane surface (inset of Fig. 1A). Photoexcitation of Lamb waves is based on two competing effects: the deformation potential mechanism and thermal expansion due to electron-phonon coupling (*10*, *27*). Each pump pulse excites electron-hole pairs that cause strain by modulating the bonding of atoms (*10*). The abrupt strain formation sets confined acoustic modes, i.e., dilatational Lamb waves, in motion (Fig. 1C). To compensate for relaxation via phonon damping and electron-hole recombination, the excitation is replenished every 12.5 ns. The high-repetition pump pulses establish a steady, nonequilibrium state that gives detectable inelastic scattering spectra of nonthermal Lamb modes. The term nonthermal denotes the coherence of photoexcited Lamb waves (Fig. 1C), in contrast with thermally populated waves that are incoherent. In the following, the coherent nature of photoexcited Lamb waves and their propagation will be studied through the lineshape and the Stokes and anti-Stokes intensities of the BLS spectra, respectively. The combination of pulsed photoexcitation of coherent acoustic phonons, with a CW-based, Brillouin scattering probe, will be termed pumped BLS.

For unexcited Si nanomembranes at room temperature, the Lamb waves under consideration are heavily occupied and can be detected

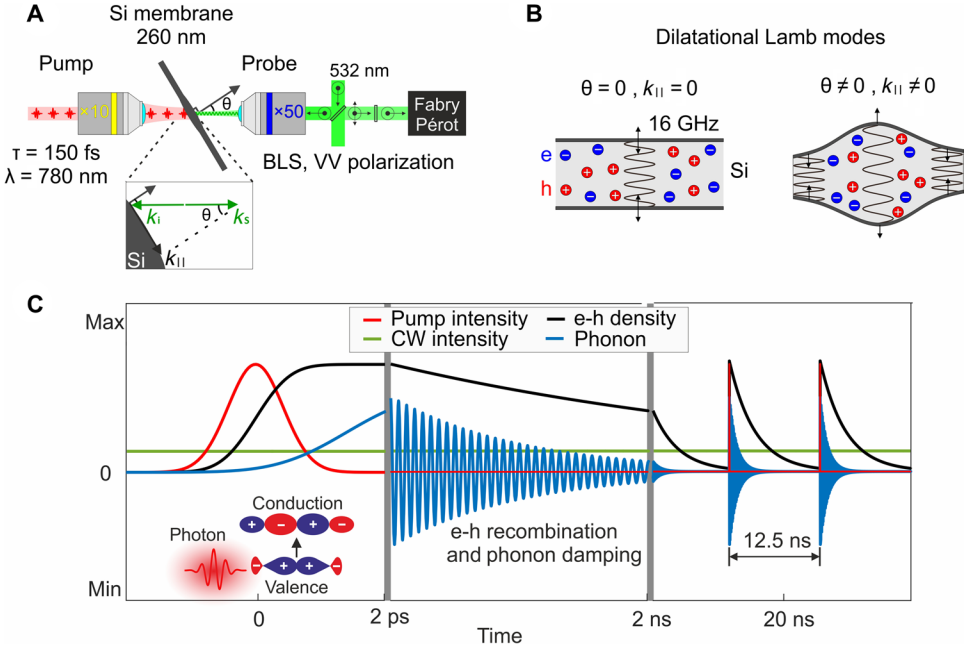

Fig. 1. Hybrid pulsed photoexcitation and frequency-domain detection of gigahertz phonons in semiconducting nanomembranes. (**A**) An all-optical–based approach for enhancing and controlling the spectral shape and intensity of spatially confined gigahertz acoustic signals. The femtosecond pulses are focused on a semiconducting nanomembrane (260 nm Si). The continuous wave (CW) laser light (532 nm) is inelastically scattered by both photoexcited and thermal phonons, and the spectrum is recorded by Brillouin light spectroscopy (BLS) at backscattering. (**B**) Illustration of the S1 dilatational Lamb waves and the coexisting electron-hole pair excitations. Standing (B, left) or propagating (B, right) waves are observed for normal incidence of the CW laser or for titled samples, respectively. (**C**) High-repetition pump pulses (red) create a nonequilibrium state of photoexcited Lamb modes (blue) and electron-hole pairs (black). The excitation is replenished by the pump pulses every 12.5 ns so that the nonequilibrium Lamb modes can produce detectable inelastic scattering of the CW laser (green).

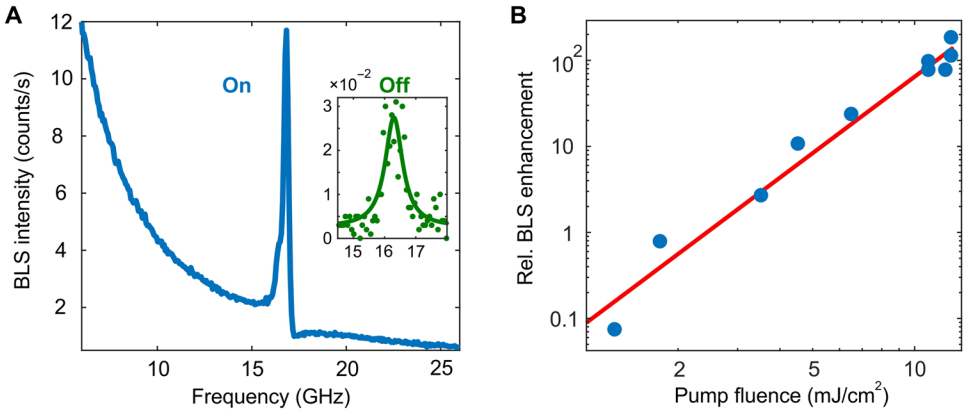

Fig. 2. Pulsed photoexcitation of dilatational, standing Lamb waves. (**A**) With the pump pulses on and at maximum power, the BLS spectrum (Stokes side) displays an intense, strongly asymmetric peak (blue curve). The maximum intensity experiences 330-fold enhancement compared with spontaneous BLS (inset). (**B**) BLS enhancement as a function of the pulse laser fluence, *F*. The red solid line denotes the representation of the experimental enhancement of the integrated peak intensity (blue points) by βF^n, where $n = (2.9 \pm 1.3)$.

through spontaneous BLS (*4*), but the BLS signal is weak. Figure 2A shows the pumped BLS spectrum (Stokes side) of the Si nanomembrane (pump on, solid blue line). The measurement was carried out with a maximum pump power of 157 mW (see Materials and Methods). The peak of the BLS spectrum (blue line) is attributed, according to its frequency, to the S1 dilatational Lamb mode at $k_{||} = 0$. The inset figure displays the spontaneous BLS spectrum (pump off, green) in the frequency region 15 to 18 GHz. Under these conditions, the maximum intensity of pumped BLS (12 counts/s; Fig. 2A) is enhanced by about 330 times as compared with the spontaneous scattering (0.03 counts/s; inset to Fig. 2A) after the subtraction of the background.

In the following, we quantify BLS enhancement on the basis of the peak area. We first measure the peak area (A) by subtracting a smooth background and integrating the intensity from 15 to 18 GHz. The relative BLS enhancement $(A^{on} - A^{off})/A^{off}$ is displayed as a function of the pump fluence, F, (blue points in Fig. 2B). The enhancement reveals nonlinear dependence that can be represented by a power function (solid red line in Fig. 2B) of the form βF^n, where β is a constant parameter and the exponent $n = (2.9 \pm 1.3)$ quantifies the nonlinearity of the process. Such nonlinear behavior has been observed before in picosecond ultrasonics experiments with semiconductors (*10*) and laser-enhanced BLS (*15*). As the BLS intensity is proportional to the mean-squared, out-of-plane displacement (*26*), a nonlinear fluence dependence of the enhancement with an exponent $n = 2$ should be anticipated. Moreover, the BLS intensity also depends on the discontinuity of the dielectric constant at the membrane-air interface (*25*). Therefore, the additional nonlinearities observed experimentally (n~3) can originate on the modified dielectric constant of the photoexcited Si.

Fano resonances in Lamb wave spectra

For all pump fluences, the spectra of the S1 Lamb waves have a strongly asymmetric lineshape and display a dip (local minimum) on the high-frequency side (e.g., blue line in Fig. 2A), so that they cannot be represented by a Lorentzian peak profile. Figure 3A shows a Stokes component of BLS spectrum of the photoexcited S1 Lamb wave (blue symbols). The spectral shape of the corresponding peak is well represented (red solid line) by the sum of a power law

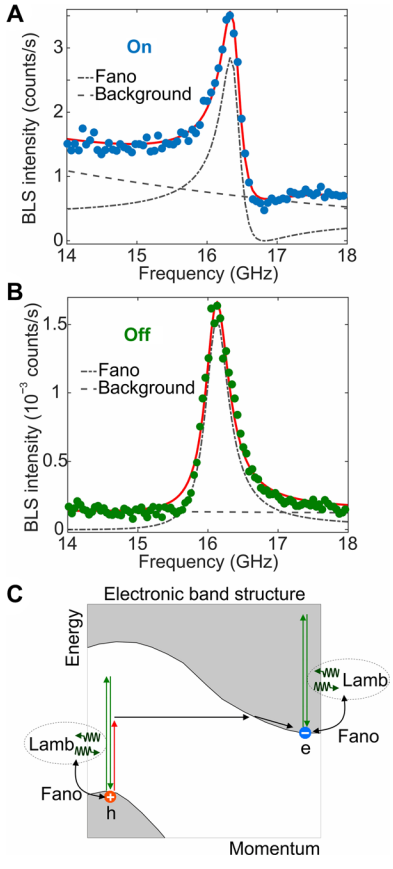

Fig. 3. Photoinduced spectral asymmetry of S1 Lamb waves. The BLS spectrum of the S1 wave (Stokes at $k_{||} = 0$) recorded in backscattering geometry when the pump pulses are either on (**A**) or off (**B**). The solid red line in (A) and (B) denotes the representation of both spectra by the sum of a smooth background (dashed) and a Fano resonance profile (dashed dot). (**C**) Scheme explaining the origin of the Fano resonances in Si membranes. Vertical colored arrows denote optical transitions with the pump (red) and the probe (green) in the electronic band structure of Si. Black arrows show how the pump transfers electrons to the conduction band (holes in the valence band). The zigzag arrows denote Stokes and anti-Stokes scattering of S1 Lamb waves. Fano coupling takes place between photoexcited Lamb modes and electron-hole pairs.

for the background ($cf^d + e$) (gray dashed line) and a Fano peak profile (gray dash-dot line) given by

$$I = I_o \frac{(a\Gamma/2 + f - f_o)^2}{(\Gamma/2)^2 + (f - f_o)^2}, \quad (1)$$

where f is the frequency, I is the intensity, f_o, I_o, and Γ are the position, the amplitude, and the width of the peak, respectively, and a is the Fano asymmetry parameter. For $|a| \to \infty$, the Fano resonance assumes a Lorentzian spectral shape. For small $|a|$ values, Eq. 1 produces a characteristic deep in the background, at the vicinity of the peak frequency. For the spectrum of Fig. 3A, $a = (2.6 \pm 0.1)$.

The emergence of Fano peak profiles is due to the coupling of a well-defined resonance with a continuum of background excitations (*28*). The coupling strength between the resonance and the continuum can be expressed by $1/|a|$. Previous reports based on Raman spectroscopy of Si nanostructures have shown that Fano resonances of optical phonons can simply arise by increasing the irradiation power of a CW laser (*29*). On the contrary, the Fano spectral shapes in the present BLS experiments are exclusively induced by the pump pulses as demonstrated in Fig. 3B that shows an experiment using only the CW beam (pump laser off). The BLS spectrum, due to spontaneous scattering by thermal phonons, shows only a weak asymmetry of opposite sign. Using the same fitting procedure as in Fig. 3A, the Fano asymmetry parameter is now $a = (-15.48 \pm 0.01)$. Using a total of seven pump-on and -off measurements (Supplementary Materials, fig. S4), the absolute Fano coupling strength shows a pump-induced, fivefold enhancement from $1/|a| = (0.07 \pm 0.03)$ for spontaneous BLS, to $1/|a| = (0.33 \pm 0.10)$ for pumped BLS. Hence, strongly asymmetric Fano resonances are solely observed following excitation by ultrashort pump pulses and remain unseen for CW light irradiation only. This observation corroborates the notion of a photoinduced and nonthermal phenomenon.

Interpretation of Fano resonances

To understand the origin of the Fano resonances, we need to indicate a microscopic subsystem of Si that can act as a continuum of background excitations. We consider the possibility of Fano coupling between S1 Lamb waves and electron-hole pair excitations and set two criteria. The electron-hole pair excitations must be impulsive, and their lifetime must be in the nanosecond range to allow for energy exchange with the Lamb modes. The first criterion is warranted by the ultrashort pump pulses (150 fs), which are significantly shorter than the S1 Lamb mode period (62.5 ps). The second criterion should be examined for the specific Si membranes used in the experiments, as electron-hole recombination is very sensitive to surface roughness and contamination. Therefore, we have used optical pump-THz probe (OPTP) spectroscopy (*30*) to characterize the Si membranes used in our experiments (fig. S5 and relevant discussion). These experiments reveal that the lifetime of electron-hole pairs substantially exceeds 1 ns, enabling prolonged interaction with the S1 Lamb modes (*5*).

The observed Fano coupling is thus attributed to S1 waves and electron-hole plasma, as shown schematically in Fig. 3C. The direct and indirect gaps of Si are 3.2 and 1.12 eV, respectively. The incident 1.6 eV photons (vertical red arrow in Fig. 3C) transfer electrons 0.48 eV above the conduction band minimum. The transfer of electrons to the conduction band is a phonon-assisted process (horizontal black arrow in Fig. 3C). The excited electrons thermalize rapidly and relax very close to the conduction band minimum by electron-phonon coupling (tilted black arrow in Fig. 3C). The electron-phonon coupling drives the excited charge carriers in equilibrium with the vast majority of the phonon modes within subpicosecond time scales (*31*).

The resulting abrupt heating and thermal expansion are partially driving the generation of dilatational Lamb waves in a process known as thermoelastic effect. In addition, the Si structure can have a different bonding character after the electrons are promoted from the valence band to the conduction band. Thus, photoexcitation alters the structural properties of Si for several nanoseconds (lifetime of electron-hole pairs) and can lead to displacive excitation of Lamb waves. Inversely, the dilatational Lamb waves modify the volume of the membrane, exert pressure on the Si lattice, and modulate the energy of electron-hole pairs. According to the standard theoretical description of picosecond ultrasonics experiments (*10*, *27*, *32*), the direct coupling between charge carriers and Lamb waves is described by the deformation potential mechanism, and it is enabled once the band gap (E_g) is affected by the pressure (p). The strain formation after photoexcitation is then proportional to the derivative: dE_g/dp.

The generation of Lamb waves can be impulsive or displacive, resulting in phases of 0° (sine wave) or 90° (cosine wave), respectively. The Fano resonance occurs due to interference of a well-defined resonance with a continuum of background excitations (*28*). Hence, the Fano coupling strength contains information about the phase of the Lamb waves (*33*). According to the experimentally constrained, theoretical calculations of Misochko and Lebedev (*34*), the Fano coupling strength ($1/a$) gives the phase of the photoexcited phonons (φ) though the relationship $\varphi = \arctan(-1/a)$. The phase of the photoexcited phonons can be either positive, as in the Peierls distorted semimetal Bi, or negative, as for instance for optical phonons in Si (*34*). In the fluence regime of 4 to 13 mJ/cm^2, the average phase of the S1 Lamb waves probed by pumped BLS is $\varphi = (-18 \pm 5°)$. The measured phase indicates that the Lamb waves are generated by a mixture of impulsive lattice expansion and displacive lattice shrinkage. This conclusion is consistent with previous, time-domain investigations of coherent acoustic phonons in Si (*10*, *27*). For the phase to be −18°, the amplitude for the impulsive expansion needs to be three times larger than the amplitude of displacive shrinkage (see also section S3).

To understand the broad background of the spectra, it is important to consider the detection process. The photons of the CW probe beam induce virtual transitions (vertical green arrows in Fig. 3C) of the pump-excited electrons and holes, as well as inelastic light scattering from Lamb modes (zigzag arrows in Fig. 3C). The broad background (Fig. 2A) is attributed to the quasi-elastic scattering of the CW probe from the electron-hole plasma. Huang *et al.* (*35*) have observed a broad background in the Raman spectrum of laser-excited, metallic nanoparticles in the 0 to 250 meV energy range (0 to 60 THz) because of inelastic light scattering by free charge carriers. Here, the observed background is qualitatively similar; however, the charge carrier density, as well as the investigated energy range (0 to 100 μeV), is significantly smaller. For the highest used pump fluence, the density of excited charge carriers in the Si membrane is estimated to be 1.4×10^{19} cm^{-3}. This quantity has been extracted from terahertz time-domain spectroscopy experiments, based on the thin-film approximation (*36*) and fitting the obtained frequency-resolved conductivity to the Drude model (see fig. S6 and S7) (*30*, *37*).

Another interesting possibility given by the analysis of the Fano lineshapes is to extract the lifetime of the S1 Lamb waves. The finite lifetime of photoexcited phonons stems from dissipative processes,

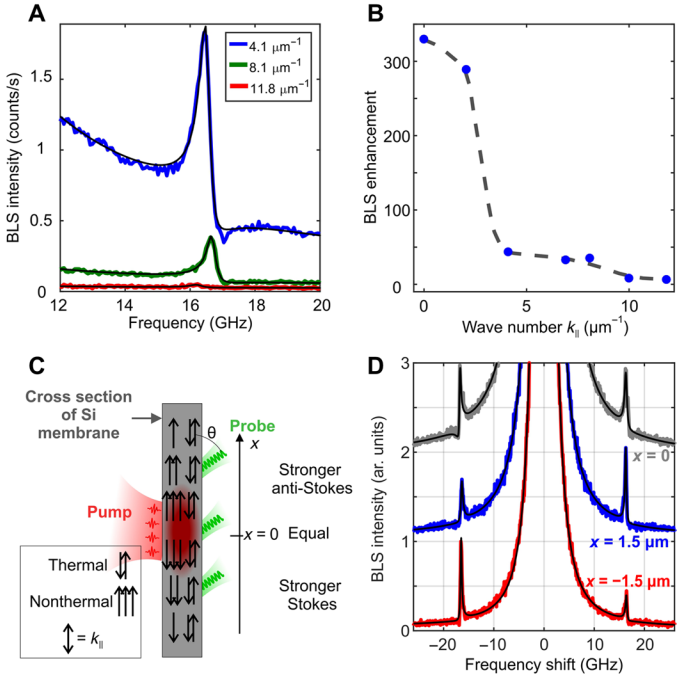

Fig. 4. Photoexcitation and detection of propagating Lamb waves. (**A**) BLS spectra of pumped photoexcited Lamb modes at various momenta. (**B**) BLS enhancement (solid symbols) as a function of the Lamb wave number $k_{\|}$ being parallel to the Si membrane. The dashed line is to guide the eye. (**C**) Scheme of the experimental geometry for generating and detecting directional currents of Lamb waves. (**D**) Pumped BLS spectra recorded at an oblique angle of θ = 17° demonstrating asymmetry of either the Stokes or anti-Stokes side of the spectrum. When the pump and probe overlap spatially (gray curve), the Stokes and anti-Stokes intensities are equal. Spatial displacement of the probe beam by $x = \pm 1.5$ μm relative to the pump (blue and red curves) causes an asymmetry of the Stokes and anti-Stokes intensities. The spectra are normalized and vertically displaced for clarity. ar. units, arbitrary units.

such as electron-phonon and phonon-phonon coupling, as well as dephasing. For the spectrum of Fig. 3A, and taking into account the instrumental broadening [full width at half maximum (FWHM) = 0.29 GHz; see also fig. S9 and relevant discussion], the width of the S1 resonance is 0.14 ± 0.01 GHz. The corresponding lifetime is 7.1 ± 0.5 ns, in reasonable agreement with the work of Cuffe *et al.* (*5*). Up to this point, all the analyses are based on standing Lamb waves ($k_{\|} = 0$). Because of the lack of momentum resolution in most pump-probe optical spectroscopies, it remains unclear if photoexcitation by means of a single Gaussian beam can launch in-plane propagating acoustic waves in addition to standing waves (*5*).

Propagating Lamb waves and momentum-resolved measurements

To explore the full potential of BLS in combination with pulsed photoexcitation, we now turn to momentum-resolved measurements by increasing the angle of incidence θ (Fig. 1A). Figure 4A displays pumped BLS spectra recorded for various θ and, hence, wave numbers of the Lamb modes. Both the BLS intensity enhancement and the asymmetric Fano profile are evident also at $k_{\|} \neq 0$. The BLS enhancement as a function of the wave number $k_{\|}$ is displayed in Fig. 4B. The BLS enhancement exhibits a rapid drop from 100-fold to 10-fold at $k_1 \sim 3\ \mu m^{-1}$ and vanishes above $k_2 \sim 10\ \mu m^{-1}$. The corresponding lengths in real-space are $2\pi/k_1 \sim 2$ μm and $2\pi/k_2 \sim 600$ nm. The experimental results of Fig. 4 (A and B) illustrate that pulsed photoexcitation coupled to BLS can generate and probe propagating acoustic phonons ($k_{\|} \neq 0$) besides standing waves ($k_{\|} = 0$).

For various experiments and applications, it is desirable to generate streams of Lamb waves with clear directional transport, meaning broken left-right symmetry. Here, the left-right symmetry is strongly violated in the vicinity of the pumped area. This enables the observation of directional transport of Lamb waves by displacing the pump and probe beams. The displacement of the probe beam is parallel to the membrane surface and on the plane of the angle θ (x axis in Fig. 4D). In the vicinity of the irradiated area, the preferential motion of phonons away from the pumped area manifests as an asymmetry of the Stokes and anti-Stokes peak intensities—displayed in Fig. 4C (θ = 17°). At larger distances, the signal is dominated by thermal phonons without left-right asymmetry. When the pump and the probe overlap ($x = 0$), the Stokes and anti-Stokes intensities are comparable (gray points in Fig. 4D). Spatial displacement of the probe beam by $x = +1.5$ μm or $x = -1.5$ μm leads to BLS spectra with excess anti-Stokes (blue points in Fig. 4D) or excess Stokes intensities (red points in Fig. 4D), respectively. The asymmetry of the Stokes and anti-Stokes intensities is in the order of ~20% per 1 μm of pump-probe displacement (fig. S10). The directional transport is not a trivial consequence of heat gradients because that would require a thermal distribution of all Lamb modes. Instead, the pump pulses specifically excite S1 waves. The relaxation lifetimes of standing Lamb modes, photoexcited by Gaussian-shaped laser pulses, can be affected by energy leakage due to propagating Lamb modes. Thus, it is desirable to reexamine the phonon lifetimes measured by time-resolved optical measurements (*5*), taking into account propagating acoustic waves as an additional pathway for energy dissipation.

DISCUSSION

The generation of coherent hypersonic phonons is usually based on prescribed metallic transducers (*15*) or coherent, extreme ultraviolet pulses (*11*, *12*). Our work enables a table-top, transducer-free method for amplification and ultrasensitive detection of standing and propagating gigahertz acoustic waves in spatially confined structures. The developed method combines the ultrafast generation of coherent acoustic phonons with inelastic, Brillouin scattering of a CW photon source. In the absence of ultrashort pulses, the phenomenon of Brillouin scattering itself is known to generate acoustic phonons (stimulated BLS), and it is used in a variety of chip-sized acousto-optic devices (*38*). However, stimulated BLS uses CW laser sources that generate acoustic phonons of well-defined frequency and momentum, and it is applicable for bulk materials, optical fibers, or waveguides that are transparent. In contrast, pump-BLS uses a broad bandwidth, optical excitation that generates Lamb waves in an extended part of the phonons' band structure (Fig. 4B). Moreover, it is used on (semi)opaque, semiconducting materials with strong spatial confinement. Because of the semiconducting properties of the investigated samples, pumped BLS can probe interactions of charge carriers with acoustic phonons. In stimulated BLS, the photons interact directly with phonons with electrostrictive forces (*38*) and in the absence of electronic excitations.

The investigated nanomembranes are frequently used as integral building blocks of more complicated, heterogeneous phononic structures, such as supported colloidal crystals (*39*) and other 2D phononic or optomechanical crystals (*2*). In addition, pumped BLS is expected to be readily applicable to other narrow-band-gap semiconductors,

such as ultrathin, layered transition metal dichalcogenides, which so far have been measured only with spontaneous (thermal) BLS (*40*), and heterostructures of layered materials (*41*). Thus, the presented method is applicable to a wide variety of functional nano- and metamaterials. The ability of pumped BLS to probe nonequilibrium states of phonons and charge carriers in the frequency domain is based on the proximity of the lifetimes of phonons (7 ns) and excited carriers (5 ns) to the repetition rate of the pump pulses (12.5 ns). The lifetime of excited carriers is highly sensitive to the surface morphology and composition, while the phonon lifetimes can drastically change with the membrane thickness. Therefore, the applicability of pumped BLS can be further extended by tuning the repetition rate of the pump laser (e.g., with pulse pickers) and by performing time-resolved BLS measurements, with a resolution of ~0.1 to 1 ns, using conventional electronic triggering of the BLS photodetector.

Moreover, photoexcitation was shown to actively switch the spectrum of gigahertz phonons from quasi-Lorentzian to Fano. Previously, active control of phonons with light has been demonstrated for high-energy vibrations, such as optical phonon-polaritons (*42*, *43*). The direct, frequency domain observation of Fano resonances between acoustic phonons and charge carriers bears direct relevance for applications at the interface of phononics and optoelectronics. The interaction of acoustic phonons with electronic degrees of freedom plays a crucial role in the mobility of charge carriers (*32*) and the lifetimes of coherent gigahertz phonons (*44*). Previously, Fano resonances of acoustic phonons in photoexcited semiconductors (GaAs) have been detected indirectly from Fourier-transformed, time-resolved data (*45*) with fixed momentum. More broadly, acoustic Fano resonances have been associated with the formation of hybridization band gaps (*39*, *46*), and thus, they can play an important role in the engineering of phononic band structures. The presently reported Fano-type interaction of dilatational Lamb waves with charge carriers suggests that well-known methods in electronics, such as doping and plasmonic enhancement, might also be useful for tailoring the performance of phononic devices. In reverse, phononic Fano resonances can be used to study electronic properties such as carrier concentrations (*47*).

In addition, we have shown that photoexcitation generates both standing and propagating Lamb waves. Directional phonon transport was shown through a spatial displacement of the pumped and the probed sample areas. The spatial distribution and propagation of the photoexcited Lamb waves could potentially be controlled by pulse shaping of the pump laser. Previous works that investigated the lifetimes of confined acoustic phonons (*5*) observed experimentally purely standing waves. Hence, the effect of phonon transport parallel to the membrane, which was observed here, was not taken into account. The observed coupling between Lamb waves and electron-hole pair excitations should also have an effect on the lifetime and dynamics of acoustic phonons in spatially confined semiconductors.

Regarding applications, pumped BLS can be used (i) for characterization of semiconducting nanomaterials with poor signal-to-noise ratio for conventional, spontaneous BLS, (ii) as a frequency-domain probe of nonthermal, carrier-lattice states in semiconductors, and (iii) as a versatile source of coherent phonons in nanodevices. Being able to generate and observe currents of gigahertz acoustic phonons on ultrathin membranes paves the way for many interesting experiments and applications in the field of phononics. The control of coherent hypersonic phonons with light is important for signal processing (*1*, *2*) and information storage devices (*48*, *49*). Momentum-resolved studies of photoexcited gigahertz phonons can reveal the effect of nanomechanical motions and hypersound on the properties of systems with strong light-matter interactions, such as polar dielectric (*50*) and plasmonic (*51*) metamaterials. Last, the laser-generated phononic wave packets can be used to study topological phononic structures and phonon localization (*52*) or phonon diodes with strictly directional phonon transport in topological structures (*53*), and to prove acoustic Anderson localization (*54*) for hypersound in 2D disordered materials.

MATERIALS AND METHODS

Sample

The Si membrane (Norcada) has a thickness of 260 nm and an area of ~2 × 2 mm2; it is suspended on a square Si support, and the sample holder is mounted on a translational and rotational stage. Silicon is lightly doped with boron, and the membrane surface is parallel to the (001) plane of Si.

μ-BLS measurements

The CW probe has a wavelength of 532 nm, and it is focused with a microscope objective (Nikon) with ×50 magnification, 0.40 numerical aperture (NA), and 22.00-mm working distance (WD). The μ-BLS measurements were carried out with the vertical-vertical or VV (*ss*) polarization of the incident and scattered light, respectively. For most measurements, the in- and out-coupling pinholes of the spectrometer (high-contrast tandem Fabry-Pérot interferometer) were 300 and 450 μm, respectively; the interferometer mirror spacing was set to 5 mm, and the scanning amplitude was 490 nm, allowing us to measure in the ±24.05-GHz frequency range. An exception to these is the CW-only spectrum in Fig. 3B, which was measured at a narrower frequency range (denser data points) to resolve more subtle peak asymmetries.

Pump

Pump pulses of 780-nm central wavelength (1.6-eV photon energy) emerge from a femtosecond laser system (TOPTICA Ultra 780) with 150-fs pulse duration, 80-MHz repetition rate, and a maximum power of 500 mW. For the presently reported experiments, the maximum power was 157 mW. The pump pulses are focused on the Si membrane with a microscope objective (Nikon) of ×10 magnification, NA 0.22, and WD of 10.5 mm. For the measurements of the Stokes/anti-Stokes asymmetry, the optics for focusing the pump were displaced with a motorized linear stage (piezo stepping drive, NEXACT N565).

Fluences of probe and pump beams

The CW probe is focused with a microscope objective to a spot with radius (1.6 ± 0.5) μm (4σ). For the pump-probe experiments, the incident CW power is (0.78 ± 0.01) mW, corresponding to a fluence of $(4 \pm 2) \cdot 10^4$ W/cm^2. The focus of the pump pulses has a Gaussian profile with radius (4.3 ± 0.2) μm. The maximum, incident, pump power is (157.0 ± 0.1) mW, which corresponds to a maximum fluence of (12 ± 1) mJ/cm^2. The uncertainties of the pump and probe fluences stem mainly from the accuracy in measuring the focus areas.

Pump-BLS measurements

The measurement of Fig. 2A used a pump fluence of 12.3 mJ/cm^2, a CW probe fluence of $3.8 \cdot 10^4$ W/cm^2, and an exposure time of 38 min. The measurement of Fig. 3A used a pump fluence of 12.8 mJ/cm^2, CW probe fluence of $3.8 \cdot 10^4$ W/cm^2, and exposure time of 4 min

(maximum intensity, 3.5 counts/s). The measurement of Fig. 3B was carried out with long exposure time (9 hours) at a power of 2 mW ($9.7 \cdot 10^4$ W/cm^2).

Statistics

For fitted quantities, the errors represent the 68.2% confidence intervals ($\pm\sigma$) of the corresponding fittings. For values that are calculated from fitted quantities, the errors are propagated accordingly. For instance, the Fano couplings ($1/|\alpha|$) have errors $\delta(1/|\alpha|) = \delta\alpha/\alpha^2$, where $\delta\alpha$ are the fitting errors of the Fano asymmetry factor α. When a quantity comes from averaging of n values, the error is the SD of these n values.

SUPPLEMENTARY MATERIALS

Supplementary material for this article is available at http://advances.sciencemag.org/cgi/content/full/6/51/eabd4540/DC1

REFERENCES AND NOTES

1. S. Volz, J. Ordonez-Miranda, A. Shchepetov, M. Prunnila, J. Ahopelto, T. Pezeril, G. Vaudel, V. Gusev, P. Ruello, E. M. Weig, M. Schubert, M. Hettich, M. Grossman, T. Dekorsy, F. Alzina, B. Graczykowski, E. Chavez-Angel, J. Sebastian Reparaz, M. R. Wagner, C. M. Sotomayor-Torres, S. Xiong, S. Neogi, D. Donadio, Nanophononics: State of the art and perspectives. *Eur. Phys. J. B* **89**, 15 (2016).
2. M. Sledzinska, B. Graczykowski, J. Maire, E. Chavez-Angel, C. M. Sotomayor-Torres, F. Alzina, 2D phononic crystals: Progress and prospects in hypersound and thermal transport engineering. *Adv. Funct. Mater.* **30**, 1904434 (2020).
3. V. Romero-García, A.-C. Hladky-Hennion, *Fundamentals and Applications of Acoustic Metamaterials: From Seismic to Radio Frequency* (Wiley-ISTE, London, UK, 2019).
4. B. Graczykowski, A. Gueddida, B. Djafari-Rouhani, H.-J. Butt, G. Fytas, Brillouin light scattering under one-dimensional confinement: Symmetry and interference self-canceling. *Phys. Rev. B.* **99**, 165431 (2019).
5. J. Cuffe, O. Ristow, E. Chávez, A. Shchepetov, P.-O. Chapuis, F. Alzina, M. Hettich, M. Prunnila, J. Ahopelto, T. Dekorsy, C. M. Sotomayor Torres, Lifetimes of confined acoustic phonons in ultrathin silicon membranes. *Phys. Rev. Lett.* **110**, 095503 (2013).
6. L. Shao, S. Maity, L. Zheng, L. Wu, A. Shams-Ansari, Y.-I. Sohn, E. Puma, M. N. Gadalla, M. Zhang, C. Wang, E. Hu, K. Lai, M. Lončar, Phononic band structure engineering for high-*Q* gigahertz surface acoustic wave resonators on lithium niobate. *Phys. Rev. Appl.* **12**, 014022 (2019).
7. P. Delsing, A. N. Cleland, M. J. A. Schuetz, J. Knörzer, G. Giedke, J. I. Cirac, K. Srinivasan, M. Wu, K. C. Balram, C. Baüerle, T. Meunier, C. J. B. Ford, P. V. Santos, E. Cerda-Méndez, H. Wang, H. J. Krenner, E. D. S. Nysten, M. Weiß, G. R. Nash, L. Thevenard, C. Gourdon, P. Rovillain, M. Marangolo, J. Y. Duquesne, G. Fischerauer, W. Ruile, A. Reiner, B. Paschke, D. Denysenko, D. Volkmer, A. Wixforth, H. Bruus, M. Wiklund, J. Reboud, J. M. Cooper, Y. Q. Fu, M. S. Brugger, F. Rehfeldt, C. Westerhausen, The 2019 surface acoustic waves roadmap. *J. Phys. D* **52**, 353001 (2019).
8. A. H. Safavi-Naeini, D. Van Thourhout, R. Baets, R. Van Laer, Controlling phonons and photons at the wavelength scale: Integrated photonics meets integrated phononics. *Optica* **6**, 213–232 (2019).
9. A. Baydin, R. Gatamov, H. Krzyzanowska, C. J. Stanton, N. Tolk, Energy-dependent amplitude of Brillouin oscillations in GaP. *Phys. Rev. B* **99**, 165202 (2019).
10. P. Ruello, V. E. Gusev, Physical mechanisms of coherent acoustic phonons generation by ultrafast laser action. *Ultrasonics* **56**, 21–35 (2015).
11. J. A. Rogers, L. Dhar, K. A. Nelson, Noncontact determination of transverse isotropic elastic moduli in polyimide thin films using a laser based ultrasonic method. *Appl. Phys. Lett.* **65**, 312–314 (1994).
12. F. Bencivenga, R. Mincigrucci, F. Capotondi, L. Foglia, D. Naumenko, A. A. Maznev, E. Pedersoli, A. Simoncig, F. Caporaletti, V. Chiloyan, R. Cucini, F. Dallari, R. A. Duncan, T. D. Frazer, G. Gaio, A. Gessini, L. Giannessi, S. Huberman, H. Kapteyn, J. Knobloch, G. Kurdi, N. Mahne, M. Manfredda, A. Martinelli, M. Murnane, E. Principi, L. Raimondi, S. Spampinati, C. Spezzani, M. Trovò, M. Zangrando, G. Chen, G. Monaco, K. A. Nelson, C. Masciovecchio, Nanoscale transient gratings excited and probed by extreme ultraviolet femtosecond pulses. *Sci. Adv.* **5**, eaaw5805 (2019).
13. X. Shen, Z. Lu, Y. P. Timalsina, T.-M. Lu, M. Washington, M. Yamaguchi, Coherent phonon transport measurement and controlled acoustic excitations using tunable acoustic phonon source in GHz-sub THz range with variable bandwidth. *Sci. Rep.* **8**, 7054 (2018).
14. C.-C. Chen, H.-M. Huang, T.-C. Lu, H.-C. Kuo, C.-K. Sun, Magnitude-tunable sub-THz shear phonons in a non-polar GaN multiple-quantum-well p-i-n diode. *Appl. Phys. Lett.* **100**, 201905 (2012).
15. E. P. N. Damen, D. J. Dieleman, A. F. M. Arts, H. W. de Wijn, Generation and propagation of coherent phonon beams. *Phys. Rev. B* **64**, 174303 (2001).
16. A. Perino, Y. Shibagaki, Y. Hayashi, M. Matsukawa, Phonons induced by laser pulses for Brillouin scattering measurements. *Jpn. J. Appl. Phys.* **57**, 07LB19 (2018).
17. R. Van Laer, B. Kuyken, D. Van Thourhout, R. Baets, Interaction between light and highly confined hypersound in a silicon photonic nanowire. *Nat. Photonics* **9**, 199–203 (2015).
18. T. J. Kippenberg, K. J. Vahala, Cavity optomechanics: Back-action at the mesoscale. *Science* **321**, 1172–1176 (2008).
19. K. Hashimoto, Surface acoustic wave (SAW) devices, in *Ultrasonic Transducers: Materials and Design for Sensors, Actuators and Medical Applications*, K. Nakamura, Ed. (Elsevier, 2012), pp. 331–373.
20. K. Ishioka, A. Rustagi, U. Höfer, H. Petek, C. J. Stanton, Intrinsic coherent acoustic phonons in the indirect band gap semiconductors Si and GaP. *Phys. Rev. B* **95**, 035205 (2017).
21. R. Lu, Y. Yang, M.-H. Li, M. Breen, S. Gong, 5-GHz antisymmetric mode acoustic delay lines in lithium niobate thin film. *IEEE Trans. Microw. Theory Tech.* **68**, 573–589 (2020).
22. D. Munk, M. Katzman, M. Hen, M. Priel, M. Feldberg, T. Sharabani, S. Levy, A. Bergman, A. Zadok, Surface acoustic wave photonic devices in silicon on insulator. *Nat. Commun.* **10**, 4214 (2019).
23. B. Villa, A. J. Bennett, D. J. P. Ellis, J. P. Lee, J. Skiba-Szymanska, T. A. Mitchell, J. P. Griffiths, I. Farrer, D. A. Ritchie, C. J. B. Ford, A. J. Shields, Surface acoustic wave modulation of a coherently driven quantum dot in a pillar microcavity. *Appl. Phys. Lett.* **111**, 011103 (2017).
24. M. Weiß, H. J. Krenner, Interfacing quantum emitters with propagating surface acoustic waves. *J. Phys. D Appl. Phys.* **51**, 373001 (2018).
25. S. G. Johnson, M. Ibanescu, M. A. Skorobogatiy, O. Weisberg, J. D. Joannopoulos, Y. Fink, Perturbation theory for Maxwell's equations with shifting material boundaries. *Phys. Rev. E* **65**, 066611 (2002).
26. A. G. Every, B. A. Mathe, J. D. Comins, The study of guided waves in surfaces and thin supported films using surface Brillouin scattering and acoustic microscopy. *Ultrasonics* **44**, e929–e934 (2006).
27. O. B. Wright, V. E. Gusev, Acoustic generation in crystalline silicon with femtosecond optical pulses. *Appl. Phys. Lett.* **66**, 1190–1192 (1995).
28. U. Fano, Effects of configuration interaction on intensities and phase shifts. *Phys. Rev.* **124**, 1866–1878 (1961).
29. R. Gupta, Q. Xiong, C. K. Adu, U. J. Kim, P. C. Eklund, Laser-induced fano resonance scattering in silicon nanowires. *Nano Lett.* **3**, 627–631 (2003).
30. R. Ulbricht, E. Hendry, J. Shan, T. F. Heinz, M. Bonn, Carrier dynamics in semiconductors studied with time-resolved terahertz spectroscopy. *Rev. Mod. Phys.* **83**, 543–586 (2011).
31. M. Bernardi, D. Vigil-Fowler, J. Lischner, J. B. Neaton, S. G. Louie, Ab initio study of hot carriers in the first picosecond after sunlight absorption in silicon. *Phys. Rev. Lett.* **112**, 257402 (2014).
32. P.-A. Mante, C. C. Stoumpos, M. G. Kanatzidis, A. Yartsev, Electron-acoustic phonon coupling in single crystal $CH_3NH_3PbI_3$ perovskites revealed by coherent acoustic phonons. *Nat. Commun.* **8**, 14398 (2017).
33. D. M. Riffe, Classical Fano oscillator. *Phys. Rev. B* **84**, 064308 (2011).
34. O. V. Misochko, M. V. Lebedev, Fano interference at the excitation of coherent phonons: Relation between the asymmetry parameter and the initial phase of coherent oscillations. *J. Exp. Theor. Phys.* **120**, 651–663 (2015).
35. J. Huang, W. Wang, C. J. Murphy, D. G. Cahill, Resonant secondary light emission from Plasmonic Au nanostructures at high electron temperatures created by pulsed-laser excitation. *Proc. Natl. Acad. Sci. U.S.A.* **111**, 906–911 (2014).
36. R. E. Glover III, M. Tinkham, Conductivity of superconducting films for photon energies between 0.3 and $40kT_c$. *Phys. Rev.* **108**, 243 (1957).
37. E. Hendry, M. Koeberg, J. Pijpers, M. Bonn, Reduction of carrier mobility in semiconductors caused by charge-charge interactions. *Phys. Rev. B* **75**, 233202 (2007).
38. B. J. Eggleton, C. G. Poulton, P. T. Rakich, M. J. Steel, G. Bahl, Brillouin integrated photonics. *Nat. Photonics* **13**, 664–677 (2019).
39. B. Graczykowski, N. Vogel, K. Bley, H.-J. Butt, G. Fytas, Multiband hypersound filtering in two-dimensional colloidal crystals: Adhesion, resonances, and periodicity. *Nano Lett.* **20**, 1883–1889 (2020).
40. B. Graczykowski, M. Sledzinska, M. Placidi, D. Saleta Reig, M. Kasprzak, F. Alzina, C. M. Sotomayor Torres, Elastic properties of few nanometers thick polycrystalline MoS_2 membranes: A nondestructive study. *Nano Lett.* **17**, 7647–7651 (2017).
41. J. D. G. Greener, A. V. Akimov, V. E. Gusev, Z. R. Kudrynskyi, P. H. Beton, Z. D. Kovalyuk, T. Taniguchi, K. Watanabe, A. J. Kent, A. Patanè, Coherent acoustic phonons in van der Waals nanolayers and heterostructures. *Phys. Rev. B* **98**, 075408 (2018).
42. M. A. Huber, F. Mooshammer, M. Plankl, L. Viti, F. Sandner, L. Z. Kastner, T. Frank, J. Fabian, M. S. Vitiello, T. L. Cocker, R. Huber, Femtosecond photo-switching of interface polaritons in black phosphorus heterostructures. *Nat. Nanotechnol.* **12**, 207–211 (2017).
43. A. D. Dunkelberger, D. C. Ratchford, A. B. Grafton, V. M. Breslin, E. S. Ryland, D. S. Katzer, K. P. Fears, R. J. Weiblen, I. Vurgaftman, A. J. Giles, C. T. Ellis, J. G. Tischler, J. D. Caldwell,

J. C. Owrutsky, Ultrafast active tuning of the Berreman mode. *ACS Photonics* **7**, 279–287 (2020).
44. B. Liao, A. A. Maznev, K. A. Nelson, G. Chen, Photo-excited charge carriers suppress sub-terahertz phonon mode in silicon at room temperature. *Nat. Commun.* **7**, 13174 (2016).
45. M. Vinod, G. Raghavan, V. Sivasubramanian, Fano resonance between coherent acoustic phonon oscillations and electronic states near the bandgap of photoexcited GaAs. *Sci. Rep.* **8**, 17706 (2018).
46. F. Lemoult, N. Kaina, M. Fink, G. Lerosey, Wave propagation control at the deep subwavelength scale in metamaterials. *Nat. Phys.* **9**, 55–60 (2013).
47. T. Mitani, S.-i. Nakashima, K. Kojima, T. Kato, H. Okumura, Determination of carrier concentration by Fano interference of Raman scattering in heavily doped n-type 4H-SiC. *J. Appl. Phys.* **112**, 043514 (2012).
48. D. P. Lake, M. Mitchell, P. E. Barclay, Processing telecom wavelength light with an optically tunable memory. arXiv:1912.06118 (2019).
49. B. Stiller, M. Merklein, C. Wolff, K. Vu, P. Ma, S. J. Madden, B. J. Eggleton, Coherently refreshing hypersonic phonons for light storage. *Optica* **7**, 492–497 (2020).
50. N. C. Passler, C. R. Gubbin, T. G. Folland, I. Razdolski, D. S. Katzer, D. F. Storm, M. Wolf, S. De Liberato, J. D. Caldwell, A. Paarmann, Strong coupling of epsilon-near-zero phonon polaritons in polar dielectric heterostructures. *Nano Lett.* **18**, 4285–4292 (2018).
51. B. G. M. Vieira, N. S. Mueller, E. B. Barros, S. Reich, Plasmonic properties of close-packed metallic nanoparticle mono- and bilayers. *J. Phys. Chem. C* **123**, 17951–17960 (2019).
52. Z.-Y. Ong, C. H. Lee, Transport and localization in a topological phononic lattice with correlated disorder. *Phys. Rev. B* **94**, 134203 (2016).
53. T. Devaux, A. Cebrecos, O. Richoux, V. Pagneux, V. Tournat, Acoustic radiation pressure for nonreciprocal transmission and switch effects. *Nat. Commun.* **10**, 3292 (2019).
54. H. Hu, A. Strybulevych, J. H. Page, S. E. Skipetrov, B. A. van Tiggelen, Localization of ultrasound in a three-dimensional elastic network. *Nat. Phys.* **4**, 945–948 (2008).

Acknowledgments
Funding: This work was supported by the Polish National Science Centre (UMO-2018/31/D/ST3/03882) and the ERC AdG SmartPhon (grant no. 694977). T.V. and B.G. acknowledge the support from the Foundation for Polish Science (POIR.04.04.00-00-5D1B/18). **Author contributions:** B.G. and G.F. conceived the project. T.V. and B.G. performed the BLS measurements. H.Z., H.W., and M.B. performed the terahertz measurements. T.V., G.F., and B.G. analyzed the data, prepared the figures, and wrote the manuscript with input from all authors. All authors contributed to the discussion of the results. **Competing interests:** The authors declare that they have no competing interests. **Data and materials availability:** All data needed to evaluate the conclusions in the paper are present in the paper and/or the Supplementary Materials. Additional data related to this paper may be requested from the corresponding authors. Correspondence and requests for materials should be addressed to G.F. and B.G.

Submitted 25 June 2020
Accepted 4 November 2020
Published 18 December 2020
10.1126/sciadv.abd4540

Citation: T. Vasileiadis, H. Zhang, H. Wang, M. Bonn, G. Fytas, B. Graczykowski, Frequency-domain study of nonthermal gigahertz phonons reveals Fano coupling to charge carriers. *Sci. Adv.* **6**, eabd4540 (2020).

Science Advances

Frequency-domain study of nonthermal gigahertz phonons reveals Fano coupling to charge carriers

Thomas Vasileiadis, Heng Zhang, Hai Wang, Mischa Bonn, George Fytas and Bartlomiej Graczykowski

Sci Adv **6** (51), eabd4540.
DOI: 10.1126/sciadv.abd4540

Science Advances (ISSN 2375-2548) is published by the American Association for the Advancement of Science, 1200 New York Avenue NW, Washington, DC 20005. The title *Science Advances* is a registered trademark of AAAS.